Structural Analysis and Charge Density Study of Lithium Formate Monohydrate

J.A. van der Horn

July 29, 2015

1

Introduction

Lithium formate monohydrate (LiHCOO · H$_2$O) is known for its piezoelectric properties and its susceptibility to nonlinear optics. [1] Nowadays, it is researched mostly for applications in clinical EPR dosimetry. [2–4]

The crystal structure was first determined in 1971 and was resolved again in 1972 with better quality data. [5, 6] All known crystal structures up to now were measured at room temperature, and none of these concern the determination of the absolute structure.

In the 1970s, various $X - N$ difference density studies have been done on this compound, to gain insight in the charge density distribution in the crystal. [7–9] These kinds of studies are known to give rise to certain problems, including the interpretation of thermal motion. [10] Also, incorrect treatment of the phase problem can cause the difference density to be systematically underestimated. [10, 11]

This work deals with the question how state-of-the-art technology can improve the quality of the results of the structure determination. It is shown how high resolution data can be used to perform a topological analysis on the charge density distribution in lithium formate monohydrate and determine its absolute crystal structure.

2

Experimental

2.1 Crystallization

Crystals were made by preparing a 333 K saturated lithium formate monohydrate (Aldrich, 98%) solution in water and cooling it down to room temperature over 2 hours. Three different crystals were used in this study for the temperature dependent unit cell determination, the temperature dependent structure determination and the high resolution measurement, respectively.

2.2 Diffraction equipment

Data were obtained with a Bruker Kappa ApexII diffractometer (four circles with CCD detector) with sealed tube and Triumph monochromator, using Mo $K\alpha$ radiation. The temperature was controlled with an Oxford 700 Series Cryostream Cooler. Crystals were mounted using a MiTeGen 300 μm Dual-Thickness MicroLoop.

For the temperature dependent unit cell measurement, the crystal was attached to the loop with super glue. For the temperature dependent structure measurement and the high resolution measurement, crystals were attached to the loop with perfluoropolyalkylether (ABCR). [12]

2.3 Temperature dependent unit cell determinations

A temperature dependent measurement was done to determine how the unit cell expands when the crystal is heated up. Individual measurements were performed from T = 110 K up to T = 290 K, with 10 K difference between each measurement. Each measurement consisted of three ω-scans, with 50 images per scan. The crystal was rotated for 0.5° per frame with an exposure time of 5 seconds. The position of the detector remained fixed during the whole experiment. Reflections were recorded upto a resolution of $(\sin\theta/\lambda)_{max} = 0.62$ Å^{-1}, resulting in a total of between 449 and 456 reflections for each measurement. Peak positions were refined with the Peakref software, using a fixed detector

alignment for all measurements. [13] Peaks were integrated using the Eval15 software. [14] Cell parameters were obtained from the Peakref software.

2.4 Temperature dependence of crystal structure

Two measurements were done to gain insight in the temperature dependence of the atom coordinates in the crystal. The measurements were performed at T = 110 K and T = 210 K, respectively. Reflections were recorded up to a resolution of $(\sin\theta/\lambda)_{max} = 0.81$ Å^{-1}. Peaks were integrated using the Eval15 software. Multiscan absorption correction and scaling was performed with Sadabs. [15] Structure refinement was done using SHELXL-2014. [16] Full experimental and refinement details are given in table 2.1.

Table 2.1: Experimental and refinement details of the temperature dependence measurement of the crystal structure

	$T = 110K$		$T = 210K$	
Molecular formula	LiHCOO · H$_2$O		LiHCOO · H$_2$O	
Formula weight	69.97 $g*mol^{-1}$		69.97 $g*mol^{-1}$	
Temperature	110(2) K		210(2) K	
Wavelength	0.71073 Å		0.71073 Å	
Crystal system, space group	Orthorhombic, $Pna2_1$		Orthorhombic, $Pna2_1$	
Unit cell dimensions	$a = 9.9701(4)$	$\alpha = 90°$	$a = 9.9707(3)$	$\alpha = 90°$
	$b = 6.4078(2)$	$\beta = 90°$	$b = 6.4477(2)$	$\beta = 90°$
	$c = 4.8309(2)$	$\gamma = 90°$	$c = 4.83852(15)$	$\gamma = 90°$
Volume	308.62(2) Å^3		311.060(18) Å^3	
Z, Calculated density	4, 1.506 g/cm^3		4, 1.494 g/cm^3	
Absorption coefficient	0.147 mm^{-1}		0.146 mm^{-1}	
F(000)	144		144	
Crystal size	$0.31*0.14*0.08$ mm^3		$0.31*0.14*0.08$ mm^3	
Theta range for data collection	$3.78° - 35.00°$		$3.76° - 34.96°$	
Limiting indices	$-15 \leq h \leq 16$		$-15 \leq h \leq 16$	
	$-9 \leq k \leq 10$		$-8 \leq k \leq 10$	
	$-7 \leq l \leq 7$		$-7 \leq l \leq 7$	
Reflections collected / unique	6970 / 1352		7040 / 1363	
	$[R_{int} = 0.0136]$		$[R_{int} = 0.0141]$	
Completeness to θ_{max}	99.8%		99.9%	
Absorption correction		Semi-empirical from equivalents		
Max. and min. transmission	0.7469 & 0.6977		0.7469 & 0.7019	
Refinement method		Full-matrix least squares on F^2		
Data / restraints / parameters	1352 / 1 / 58		1363 / 1 / 58	
Goodness-of-fit on F^2	1.129		1.113	
Final R indices $[I > 2*\sigma_I]$	$R = 0.0204$		$R = 0.0233$	
	$R_w = 0.0526$		$R_w = 0.0570$	
R indices (all data)	$R = 0.0213$		$R = 0.0246$	
	$R_w = 0.0531$		$R_w = 0.0576$	
Largest diff. peak and hole	+0.282 & -0.143 $e*$Å^{-3}		+0.199 & -0.163 $e*$Å^{-3}	

2.5 High resolution measurement and refinement

Reflections were recorded up to a resolution of $(\sin\theta/\lambda)_{max} = 1.28$ Å^{-1}. Scan details are given in table 2.2. Measurement details are given in table 2.3. The completeness, redundancy and R-values by resolution shell are given in table

2.4. Peaks were integrated using the Eval15 and Saint software, respectively.
[14, 17]

Integration with Eval15 is based on the prediction of reflection profiles from first principles using the ray-tracing method. For this integration, a mosaicity of 0.20° was used. The beam divergence was simulated using a focus distance of 80 mm and a collimator diameter of 0.60 mm. The crystal shape was modeled as shown in figure 2.1. The model for the wavelength distribution consists of $K\alpha_1$ ($\lambda = 0.70930$ Å) and $K\alpha_2$ ($\lambda = 0.71359$ Å) with relative intensities 2:1 and a white background block function, as shown in figure 2.2.

For intensities with $I/\sigma_I \leq 80$ the profile integration was used. Intensities with $I/\sigma_I \geq 100$ were obtained from a box integration. In the range $80 < I/\sigma_I < 100$ intensities from profiles and box integration were interpolated linearly.

Numerical absorption correction and scaling was performed with Sadabs. [15] Equivalent reflections were defined by point group mmm for scaling and point group mm2 for the error model. Sigma correction was done according to equation 2.1. The final value for K ranges from 0.867 to 1.054. The final value for g was refined to 0.0233.

$$\sigma^2 = [K * \sigma_I]^2 + [g < I >]^2$$

Where σ = adjusted sigma

K = scaling factor

σ_I = sigma obtained from Eval15

g = intensity-based correction factor

(2.1)

Initial structure refinement, based on Eval15-integrated reflection data, was done with SHELXL-2014. [16] The result of this refinement was further refined using the XD2006 software package. [18] Refinement with XD was done on F. During all XD refinement steps, the z-coordinate of the O(1) atom was kept fixed to avoid origin shifting.

The structure was refined anisotropically using reflection data where $I_{obs} \geq 3\sigma_{obs}$. The result is shown in table 2.5 under *Anisotropic*.

Based on the previous result, high resolution data $((\sin\theta/\lambda)_{min} = 0.81$ Å$^{-1})$ were used to refine the positions and anisotropic displacement parameters of the non-hydrogen atoms, keeping the hydrogen-parameters fixed. Low resolution data $((\sin\theta/\lambda)_{max} = 0.81$ Å$^{-1})$ were used to accurately refine the positions and isotropic displacement parameters of just the hydrogen atoms, based on generalized scattering factors (converted to XD format by Pierro Macchi in 2000), which are polarized in the direction of the bond. [19, 20] From here, the hydrogen positions and displacement parameters were kept fixed, and the positions and displacement parameters of non-hydrogen atoms were included in each step.

Continuing with the result of the previous refinement, the structure was refined using a multipole model for the electron density, as described in equation 2.2. [21] The core and spherical valance scattering factors were obtained from a Clementis Hartree-Fock Wavefunction (XD option *chfw*). [22] The deformation valence scattering factors were described by single-zeta density parameters (XD option *cszd*). [22] Multipole parameters (monopole for Li; monopole and dipole

for H; monopole, dipole, quadrupole and octopole for C and O) were first refined with symmetry constraints. Based on the result of that refinement, all multipole parameters (m, d, q, o) were refined for carbon and oxygen. The result of this refinement is shown under *Multipole*.

$$\rho(\mathbf{r}) = P_{core}\rho_{core}(r) + P_{val}\kappa^3\rho_{val}(\kappa r)$$
$$+ \sum_{l=0}^{l_{max}} \kappa'^3 R_l(\kappa' r) \sum_{m=0}^{l} P_{lm\pm}Y_{lm\pm}(\Omega)$$

Where ρ = electron density
$\quad$ r = distance from nucleus
$\quad$ P = population
$\quad$ κ = expansion coefficient
$\quad$ Y = spherical harmonical function

(2.2)

The result of the previous refinement step was used to refine the kappa parameters, describing the expansion/contraction of the multipoles. These parameters were refined for all non-hydrogen atoms. The result is shown under *Kappa*.

In this last step, all reflections, including weak reflections where $I_{obs} < 3\sigma_{obs}$, were used to repeat the previous refinement, based on the last result. The kappa value for lithium was fixed during this step. The final result is shown under *Eval15, Weak refl.*

This stepwise refinement process was repeated for the Saint integration data. The final result of that refinement is shown under *Saint, Weak refl.*

Table 2.2: Scan details of the high resolution measurement

Scan numbers	Swing range (°)	Exp. time (s)	Scan rot. (°)	Gen. amp. (mA)
$1-5$	-11.7 to +10.5	1	0.50	30.00
$6-15$	-63.2 to +54.2	10	0.50	30.00
$16-37$	-89.0 to +97.5	60	0.50	30.00
$38-40$	0.0 to +9.4	1	0.30	15.00

Table 2.3: Experimental details of the high resolution measurement

Molecular formula	LiHCOO $\cdot$ H$_2$O	
Formula weight	69.97 $g * mol^{-1}$	
Temperature	110(2) K	
Wavelength	0.71073 Å	
Crystal system, space group	Orthorhombic, $Pna2_1$	
Unit cell dimensions	$a = 9.97444(6)$	$\alpha = 90°$
	$b = 6.40956(4)$	$\beta = 90°$
	$c = 4.83269(4)$	$\gamma = 90°$
Volume	308.962(4) Å^3	
Z, Calculated density	4, 1.504 g/cm^3	
Absorption coefficient	0.146 mm^{-1}	
F(000)	144	
Crystal size	$0.33 * 0.20 * 0.12\ mm^3$	
Theta range for data collection	$3.78° - 65.04°$	
Limiting indices	$-25 \leq h \leq 25$	
	$-16 \leq k \leq 16$	
	$-11 \leq l \leq 12$	
Reflections collected / unique	68460 / 5135	$[R_{int} = 0.0197]$
Completeness to $\theta = 65.04°$	96.8% (merged Friedel pairs)	
	95.2% (unmerged Friedel pairs)	

Table 2.4: Completeness of the high resolution measurement per resolution shell, based on Eval15 data after scaling with Sadabs

θ (°)	Comp. (%)	Redun.	R_{sym}	R_{meas}	R_{pim}	χ^2
24.89	100.0	26.76	0.018	0.018	0.003	0.93
32.02	100.0	18.13	0.024	0.024	0.006	1.07
37.37	100.0	18.19	0.026	0.027	0.006	1.00
41.91	100.0	14.69	0.030	0.031	0.008	0.97
46.02	100.0	12.66	0.034	0.036	0.010	0.93
49.88	100.0	10.12	0.039	0.041	0.013	0.92
53.61	99.8	7.98	0.048	0.051	0.018	1.02
57.31	97.1	6.97	0.047	0.050	0.019	1.00
61.08	99.0	6.00	0.058	0.064	0.026	0.95
65.04	57.7	3.67	0.054	0.064	0.032	0.86
65.04	95.2	13.25	0.020	0.020	0.004	0.97

Table 2.5: Refinement details of the high resolution experiment

| Integration method		Eval15				Saint
Refinement step		*Anisotropic*	*Multipole*	*Kappa*	*Weak refl.*	*Weak refl.*
Data		5023	5023	5023	5114	5094
Restraints		0	0	0	0	0
Parameters		57	118	125	125	125
Goodness-of-fit on F		3.8270	1.7496	1.4876	1.4769	1.5370
Final R values on F	R	1.70 %	0.98 %	0.89 %	0.93 %	1.08 %
	R_{all}	1.79 %	1.07 %	0.97 %	0.97 %	1.16 %
	R_w	2.03 %	0.92 %	0.78 %	0.79 %	0.67 %
Hooft y-parameter		0.04 (5)	0.05 (5)	0.03 (5)	0.03 (5)	0.06 (5)
Largest peak ($e*$Å^{-3})		0.380	0.105	0.062	0.065	0.075
Largest hole ($e*$Å^{-3})		-0.165	-0.074	-0.089	-0.090	-0.100
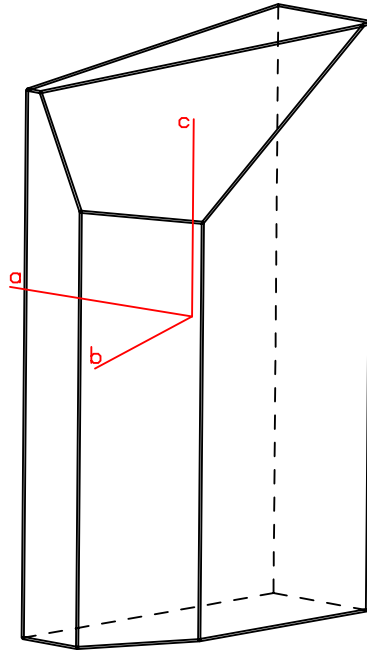
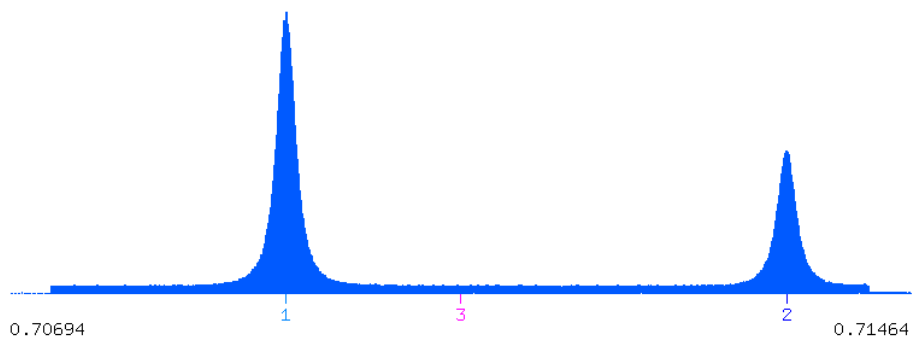Figure 2.1: Crystal shape as used for the Eval15 integration

Figure 2.2: Wavelength spectrum (Å) as used for the Eval15 integration, consisting of $K\alpha_1$, $K\alpha_2$ and white background radiation

3

Results and discussion

3.1 Temperature dependence of cell parameters

Lithium formate monohydrate crystallizes in the $Pna2_1$ space group. The crystal structure at T = 110 K is shown in figure 3.1. The structure contains a lithium ion which is tetrahedrally coordinated to four oxygen atoms. This coordination forms the basis of a polymeric chain oriented along the c-axis. In figure 3.2, the lithium ions are displayed as tetrahedrons, which shows how the asymmetric units are coordinated and packed in the unit cell. This figure also shows how the 2_1 screw axis of the space group influences the arrangement of the polymeric chains along the c-axis.

The results of the measurements are shown in table 3.1. The normalized expansion is plotted in figure 3.3. The thermal expansion is best fitted with a quadratic function, which points to long-range intermolecular interactions.

The b-axis shows a significant increase in length in this temperature range (1.17%), whereas the a-axis barely shows any expansion at all (0.05%), staying within 2σ. The expansion of the c-axis is inbetween these values (0.35%). The thermal expansion from T = 110 K to 290 K is graphically displayed as a tensor in figure 3.4. This ellipsoid shows orthorhombic symmetry, as is expected for an orthorhombic crystal system. In the next section, the origin of this behaviour is discussed.

3.2 Temperature dependence of crystal structure

Table 3.2 shows the cell parameters as well as the most important bond distances and angles by temperature. These data imply that the most important geometrical differences do not lie with the formate moiety or the lithium tetrahedron, specifically. Instead, the most significant geometrical changes are found in the hydrogen bond distances.

The individual polymeric chains are held together by two unique hydrogen bonds, as shown in figure 3.5. By hydrogen bonding, the one-dimensional coordination chain becomes a three-dimensional network structure. The hydrogen bonds are indicated in blue $(O(3) - H(3A) \cdots O(3)^\text{v})$ and pink $(O(3) -$
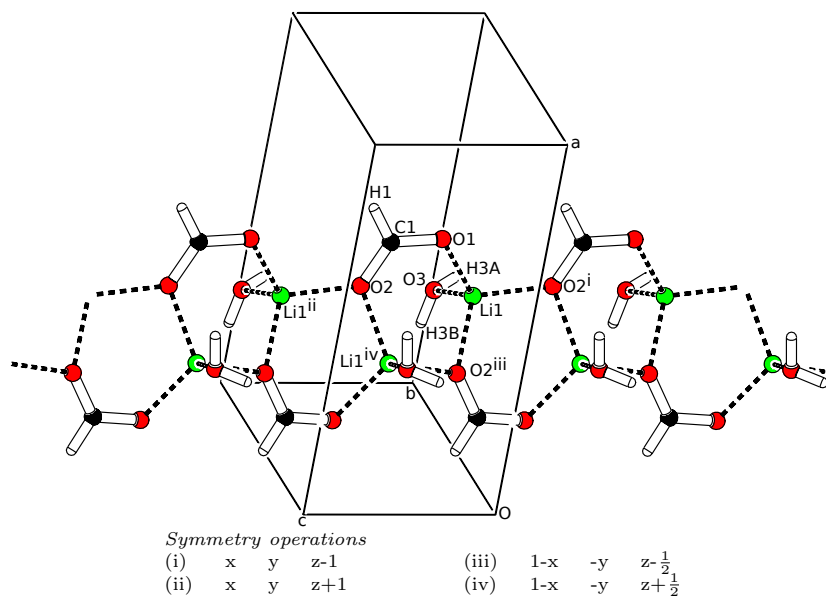
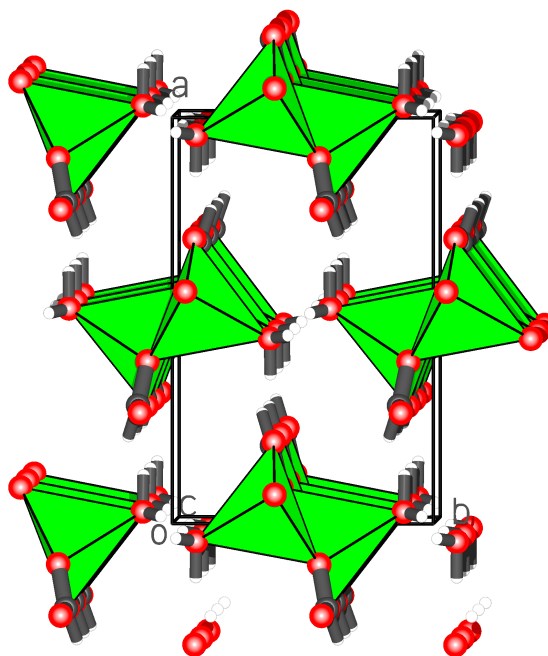Figure 3.1: Crystal structure showing the polymeric chain along the c-axis

Figure 3.2: Crystal structure viewed along the c-axis, showing coordination polyhedra and packing in the unit cell

9

Table 3.1: Cell parameters by temperature

| T (K)	a-axis (Å)	b-axis (Å)	c-axis (Å)
110	9.9809(18)	6.4133(12)	4.8349(7)
120	9.981(2)	6.4170(13)	4.8354(7)
130	9.980(2)	6.4204(10)	4.8357(7)
140	9.981(2)	6.4229(12)	4.8358(9)
150	9.981(2)	6.4278(10)	4.8367(7)
160	9.981(3)	6.4309(09)	4.8376(5)
170	9.981(3)	6.4351(11)	4.8378(9)
180	9.980(2)	6.4394(13)	4.8386(6)
190	9.980(3)	6.4429(11)	4.8397(6)
200	9.981(2)	6.4471(12)	4.8404(9)
210	9.982(3)	6.4519(13)	4.8415(7)
220	9.983(3)	6.4563(10)	4.8428(7)
230	9.983(3)	6.4603(13)	4.8442(9)
240	9.983(2)	6.4647(11)	4.8449(8)
250	9.983(2)	6.4689(13)	4.8464(8)
260	9.985(3)	6.4743(11)	4.8479(8)
270	9.985(2)	6.4788(15)	4.8485(7)
280	9.987(2)	6.4837(14)	4.8505(8)
290	9.986(2)	6.4884(13)	4.8518(9)
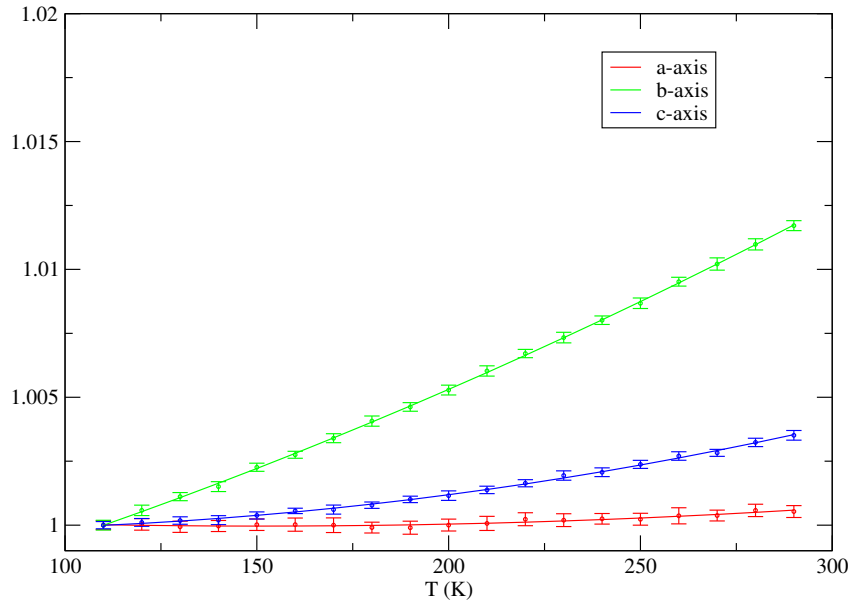
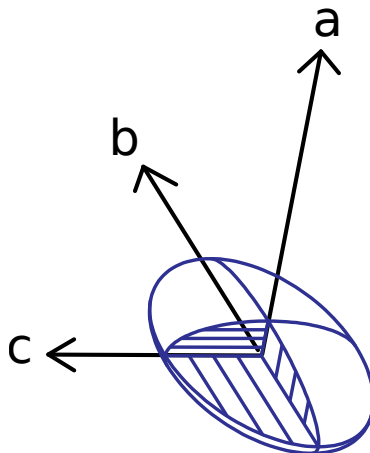Figure 3.3: Thermal expansion of lithium formate monohydrate. The normalized cell parameters are displayed.

Figure 3.4: Thermal expansion tensor for T = 110 K to T = 290 K. Expansion coefficients $\alpha_a = 3.0(16) * 10^{-6} \ K^{-1}$, $\alpha_b = 65.0(15) * 10^{-6} \ K^{-1}$ and $\alpha_c = 19.5(13) * 10^{-6} \ K^{-1}$.

$H(3B) \cdots O(1)^{\text{vi}}$), respectively. Figure 3.5c shows that the $H(3B) \cdots O(1)$ hydrogen bond is oriented in a-direction. This hydrogen bond is the shorter one and therefore also the stronger one, explaining why the unit cell barely expands in a-direction. Figures 3.5a and 3.5b show that the $H(3A) \cdots O(3)$ hydrogen bond is oriented in c-direction. This hydrogen bond is the longer one and thus the weaker one, which explains why the unit cell expands more in c-direction than it does in a-direction. The orientation of the hydrogen bonds and the difference of their strengths is thus the explanation for the thermal expansion behaviour (Section 3.1). [23]

3.3 Charge density study

3.3.1 Data and model quality

The high resolution limit of the data, with an overall completeness of 95.2%, together with an overall redundancy of 11.91, is a strong indication of high data quality. This is confirmed by the relatively small size of the displacement ellipsoids, as shown in figure 3.6.

Anisotropic structure refinement, based on Eval15-integrated data, results in an R-value of 1.70%. This value drops to 0.98% when the structure is refined using the multipole model. It is lowered even further to 0.89% when kappa-values are included in the refinement. This indicates that the multipole model provides a significantly more accurate description of the electron density than the spherical model does. The inclusion of weak reflections into the refinement provides statistical advantages, and does not degrade the accuracy of the model.

The anisotropic spherical model refinement resulted in vastly different isotropic displacement parameters for both water hydrogens, with a ratio of $U_{iso,H(3A)} : U_{iso,H(3B)} = 2.18$. After the final multipole refinement step, this ratio was decreased to 1.09. $O(3) - H(3X)$ distances were found to be 0.91 Å for both hydrogen atoms. Thomas et al. reported these distances to be 0.77

Table 3.2: Temperature dependence of crystal structure

					$T = 110\ K$	$T = 210\ K$	Δ/σ
Cell parameters (Å)							
a					9.9701(4)	9.9707(3)	+1.20
b					6.4078(2)	6.4477(2)	+141.07
c					4.8309(2)	4.8385(2)	+27.93
Formate (Å, °)							
C(1)	−	O(1)			1.2532(9)	1.2484(10)	-3.57
C(1)	−	O(2)			1.2552(9)	1.2515(10)	-2.75
O(2)	−	C(1)	−	O(1)	125.30(7)	125.50(8)	+1.88
C(1)	−	O(1)	−	Li(1)	117.94(6)	118.38(7)	+4.77
Li(1)	−	O(2)$^{\text{iii}}$	−	Li(1)$^{\text{iv}}$	101.75(7)	101.93(7)	+1.82
Li(1)$^{\text{iv}}$	−	O(2)	−	C(1)	124.86(6)	124.62(7)	-2.60
Li(1)$^{\text{ii}}$	−	O(2)	−	C(1)	130.19(7)	130.42(7)	+2.32
Lithium tetrahedron (Å, °)							
Li(1)	−	O(1)			1.9366(11)	1.9360(12)	-0.37
Li(1)	−	O(2)$^{\text{i}}$			1.9200(11)	1.9210(11)	+0.64
Li(1)	−	O(2)$^{\text{iii}}$			1.9544(11)	1.9559(12)	+0.92
Li(1)	−	O(3)			1.9661(10)	1.9717(11)	+3.77
O(1)	−	Li(1)	−	O(2)$^{\text{i}}$	111.58(8)	111.82(8)	+2.12
O(1)	−	Li(1)	−	O(2)$^{\text{iii}}$	113.19(7)	112.83(7)	-3.64
O(1)	−	Li(1)	−	O(3)	108.93(7)	108.80(7)	-1.31
O(2)$^{\text{i}}$	−	Li(1)	−	O(2)$^{\text{iii}}$	110.18(7)	110.19(7)	+0.10
O(2)$^{\text{i}}$	−	Li(1)	−	O(3)	108.90(7)	108.97(7)	+0.71
O(2)$^{\text{iii}}$	−	Li(1)	−	O(3)	103.70(7)	103.86(8)	+1.51
Hydrogen bonds (Å)							
O(3)	−	H(3A)	⋯	O(3)$^{\text{v}}$	2.8610(7)	2.8774(9)	+14.38
O(3)	−	H(3B)	⋯	O(1)$^{\text{vi}}$	2.7003(8)	2.7067(9)	+5.31

Symmetry operations

(i)	x	y	z-1	(iii)	1-x	-y	z-$\frac{1}{2}$	(v)	1-x	1-y	z-$\frac{1}{2}$
(ii)	x	y	z+1	(iv)	1-x	-y	z+$\frac{1}{2}$	(vi)	x-$\frac{1}{2}$	$\frac{1}{2}$-y	z
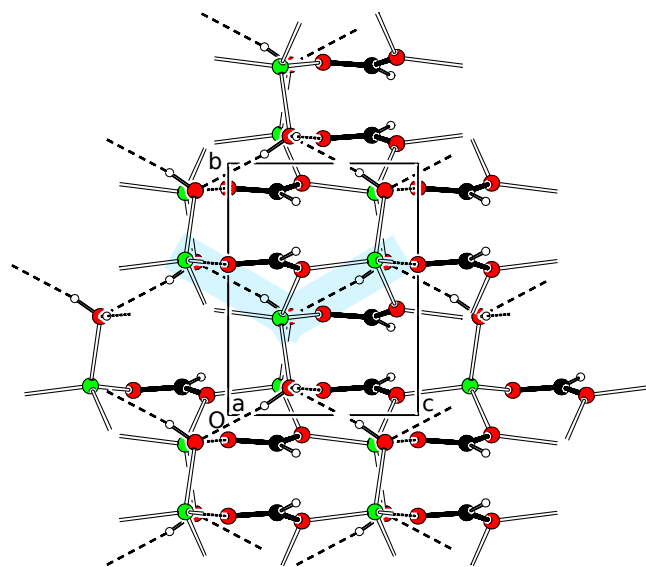
(a) View along a-axis,
indicating $O(3) - H(3A) \cdots O(3)$
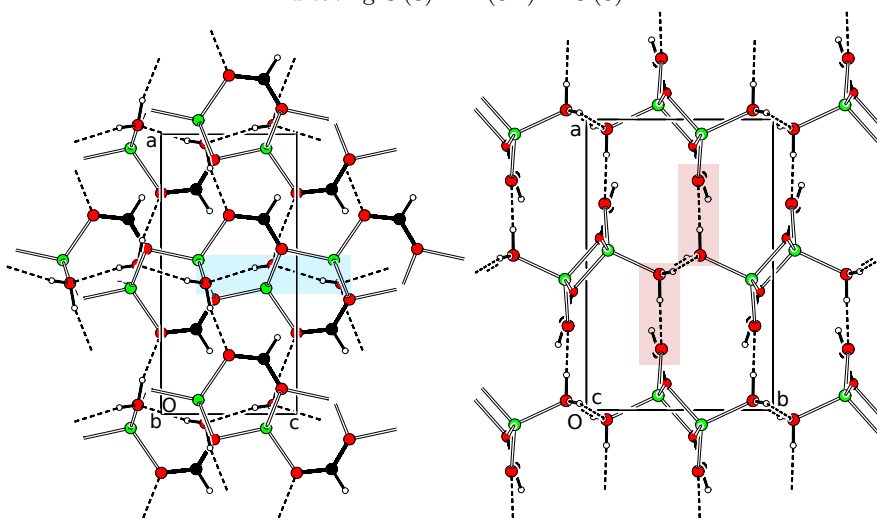
(b) View along b-axis,
indicating $O(3) - H(3A) \cdots O(3)$

(c) View along c-axis,
indicating $O(3) - H(3B) \cdots O(1)$

Figure 3.5: Crystal structure viewed along all axes respectively, indicating hydrogen bond coordinations

and 0.73 for H(3A) and H(3B), respectively, based on X-ray data, and 0.97 and 0.98 based on neutron data. [7] They ascribe these large differences to the polar character of the $O - H$ bond.

A Hirshfeld test was done on the differences of the mean-square displacement amplitudes (DMSDA) along interatomic vectors, which resulted in DMSDA values of $3 * 10^{-4}$ Å^2 and $4 * 10^{-4}$ Å^2 for O(1)→C(1) and O(2)→C(1), respectively. This indicates that the deconvolution between thermal motion and nonspherical electron density was successful.

An analysis was done on the distribution of $(I_{obs} - I_{calc})/\sigma_{obs}$ for all reflections, as shown in figure 3.7. This graph shows a near-Gaussian distribution for Δ/σ , with the exception of two outliers.

Figure 3.8 shows the distribution of I_{obs}/I_{calc} by resolution shell (3.8a) and calculated intensity (3.8b), respectively. Both graphs show a general distribution around $I_{obs}/I_{calc} = 1$. This indicates that the calculated data matches quite well with the experimental data.

The final R-value for the model based on the Eval15-integration is 0.93%. The final R-value for the model based on the Saint-integration is slightly higher, at 1.08%. Although these results are very similar, the Eval15-integration seems to give a better model in the end. This is graphically displayed in the residual density in figure 3.9. The Eval15-based model (3.9a) in particular covers most of the electron density and does not show any remaining features. Figure 3.10 shows that the intensity differences between the Eval15 and the Saint integration are most apparent for the weak reflections. This suggests that Eval15 does a better job at integrating weak reflections.
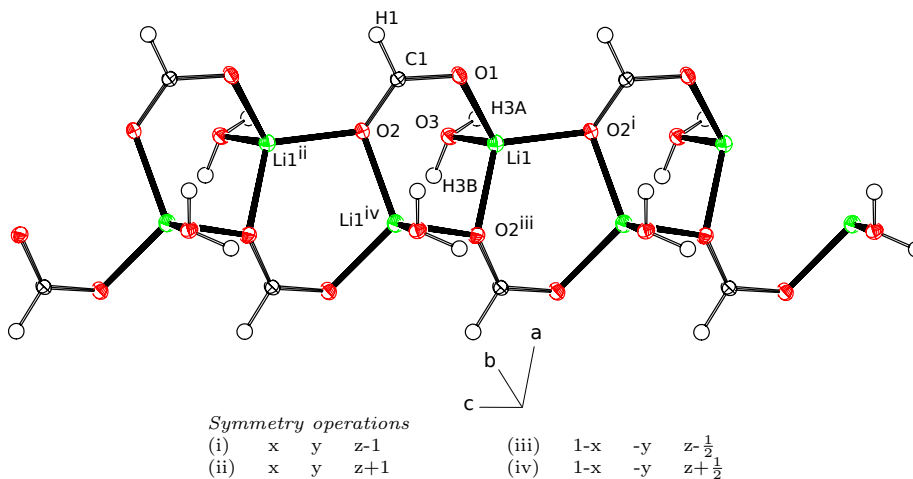

Symmetry operations
(i)   x   y   z-1   (iii)   1-x   -y   z-$\frac{1}{2}$
(ii)   x   y   z+1   (iv)   1-x   -y   z+$\frac{1}{2}$

Figure 3.6: Displacement ellipsoid plot (50% probability)

3.3.2 Absolute structure

As a consequence of its point group $mm2$, the crystal structure contains a polar axis, which is oriented along the c-axis. To determine the absolute structure of such crystals, one can analyze the intensity difference between the observed Bijvoet pairs. If the sign of the calculated intensity difference corresponds to the
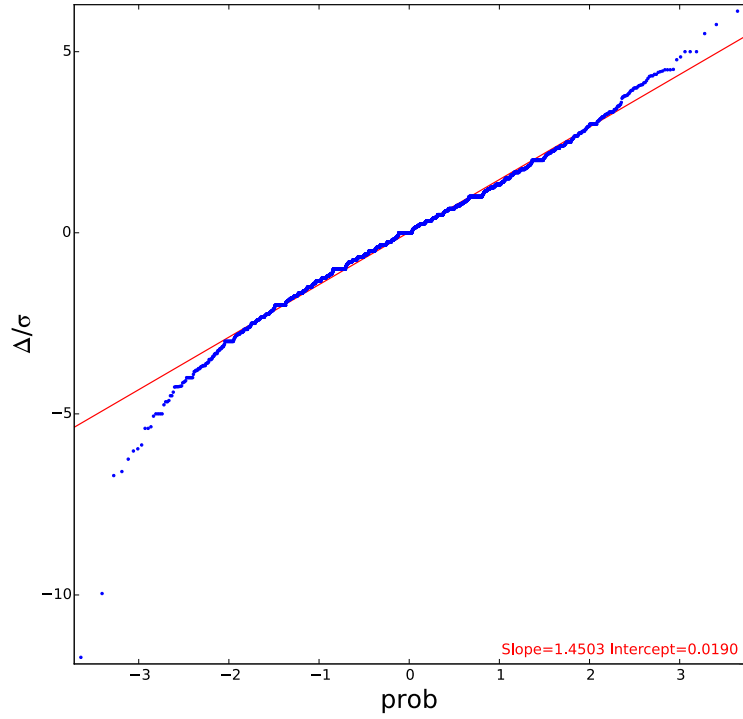
Figure 3.7: Normal probability analysis for $(I_{obs} - I_{calc})/\sigma_{obs}$
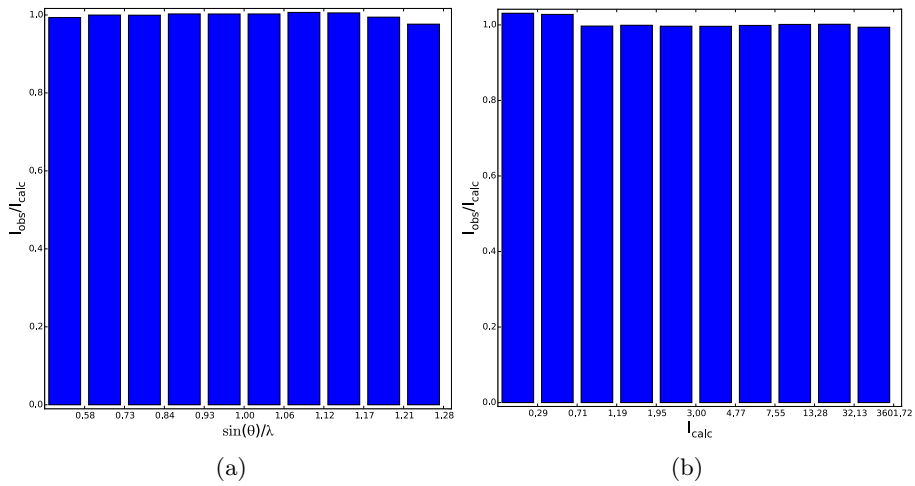

Figure 3.8: Distributions of I_{obs}/I_{calc} by resolution shell and calculated intensity, respectively
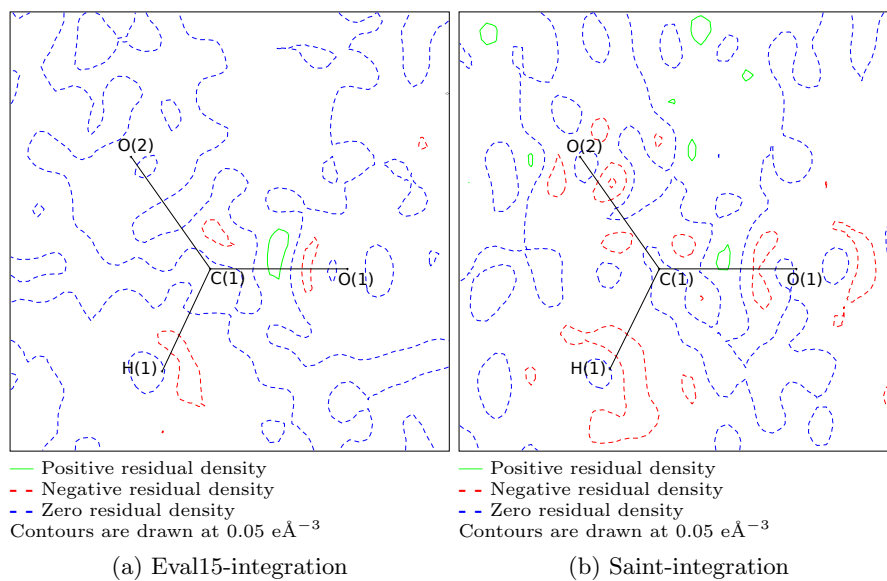
(a) Eval15-integration

(b) Saint-integration

Figure 3.9: Residual densities for models based on Eval15 and Saint integration, respectively
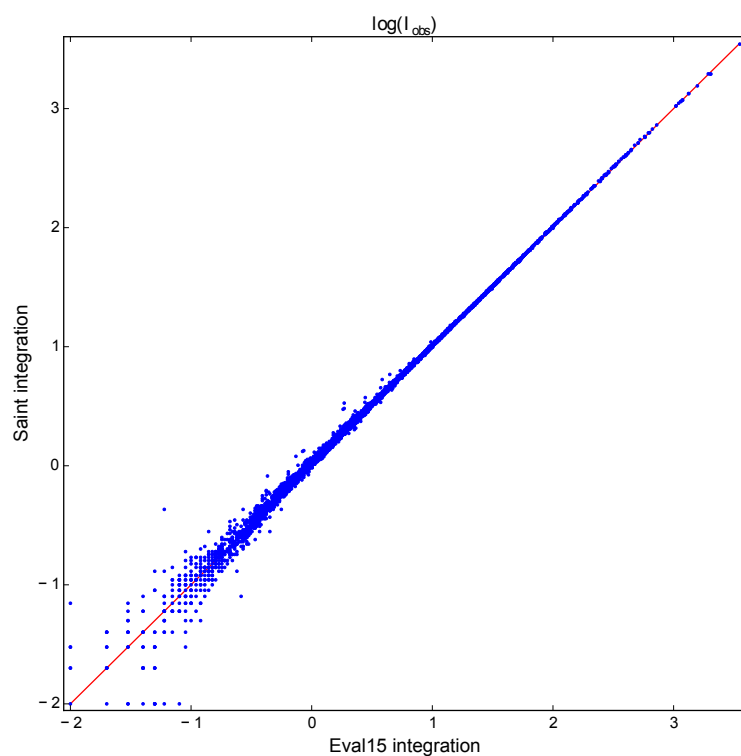

Figure 3.10: Observed intensity differences between Eval15 and Saint integration

sign of the observed intensity difference, it can be concluded that the absolute structure was determined correctly. However, the problem with this compound is that it does not contain any strong anomalous scatterers, which results in very low intensity differences between the Bijvoet pairs. This structure has a Friedif value of 6.3. [24] For comparison, the original structure of Bijvoet, sodium rubidium (+)-tartrate tetrahydrate, has a much larger Friedif value of 1096 (Mo radiation). [25] The problem is illustrated in figure 3.11.

This problem can be overcome by performing a statistical analysis on a target function, as described by equation 3.1. [26] This function describes the difference between the observed and calculated intensity differences for each Bijvoet pair. For the current structure, enantiopurity cannot be assumed a priori. The Bayesian statistics consequently has a P3 prior and leads to three different probabilities in the results. In the first place, there is the probability for the absolute structure to be determined correctly. Secondly, there is a probability that the crystal being an inversion twin. Lastly, there is the probability for the absolute structure to be incorrect.

$$z_h = \frac{\Delta F_c^2(h) - \Delta F_o^2(h)}{\sigma_{\Delta F_o^2(h)}} \quad (3.1)$$

The analysis was performed with the PLATON program on all 2352 observed Bijvoet pairs. [27] It resulted in a probability of 0.5×10^{-19} for the structure to be an inversion twin and a probability of 0.2×10^{-82} for the absolute structure to be incorrect. From this analysis, it can thus be concluded that the absolute structure was determined correctly.
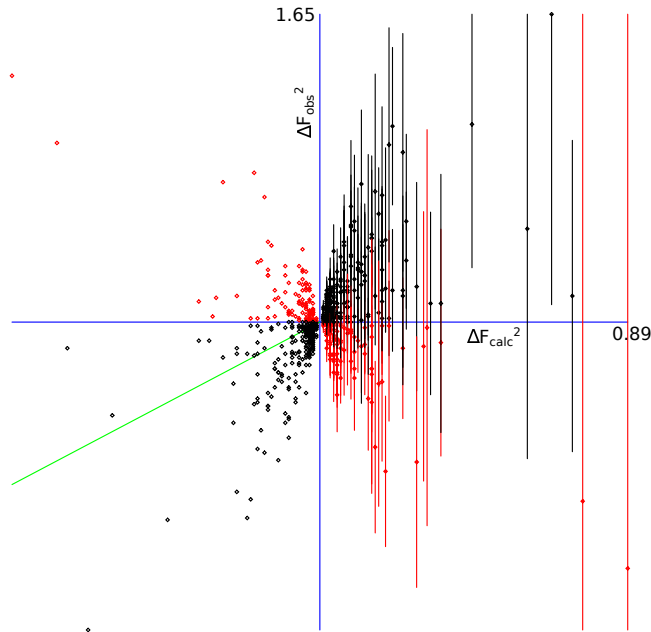

Figure 3.11: Scatter plot for 344 of the observed Bijvoet pairs ($\sigma \geq 0.25$), showing the extremely small differences between ΔF_{obs}^2 and ΔF_{calc}^2

3.3.3 Deformation density

The additional accuracy of the multipole model with respect to a spherical model can be visualized by calculating the static deformation density, as can be seen in figure 3.12a. In this graph, which shows the plane of the formate moiety, a spherical model is subtracted from the multipole model. What remains, is the non-spherical contribution to the electron density. This graph shows features like bond electrons and lone pairs on the oxygen atoms.

In 1975, an $X - N$ difference map (figure 3.12b) was obtained by Thomas et al. [7] In an $X - N$ difference map, the atomic positions and displacement parameters of the neutron experiment are used to calculate spherical X-ray structure factors F_{calc}. For the difference map, these F_{calc} are subtracted from the structure factors F_{obs}, observed in the X-ray experiment. The phase angles for F_{obs} and F_{calc} are assumed to be the same. This experiment aught to give a similar result. However, the graph they obtained does not show the aforementioned features as clearly as the calculated deformation density in this study does. This may be due to the fact that the authors had to deal with two different crystals that were used in two different experiments, which impedes the determination of the anisotropic displacement parameters. [28] Also, for non-centrosymmetric structures, this causes a significant problem for the phase determination. [7]

In the current study, the deconvolution between thermal motion and non-spherical electron density was successful.
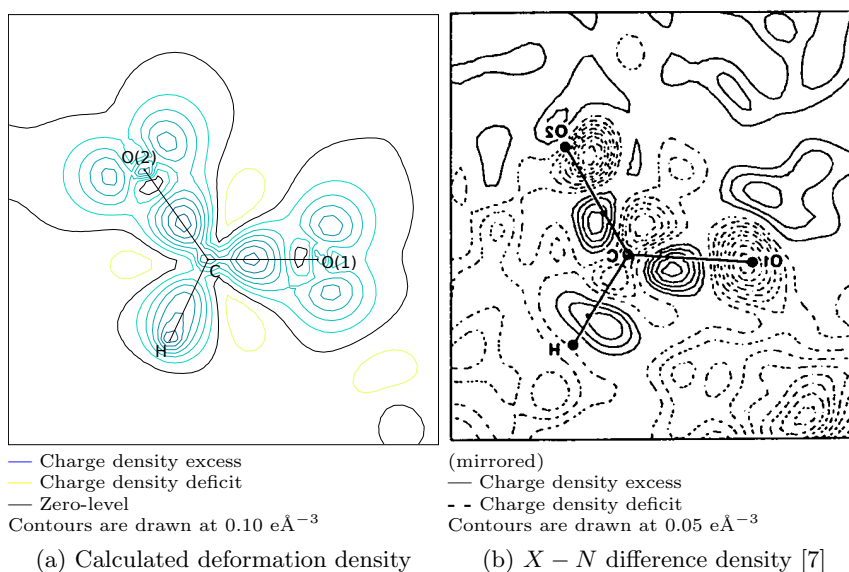

— Charge density excess
— Charge density deficit
— Zero-level
Contours are drawn at 0.10 eÅ^{-3}

(mirrored)
— Charge density excess
- - Charge density deficit
Contours are drawn at 0.05 eÅ^{-3}

(a) Calculated deformation density   (b) $X - N$ difference density [7]

Figure 3.12: Calculated deformation density compared to $X - N$ difference density obtained from literature

3.3.4 Topological analysis

A topological analysis was performed on the total electron density, as modeled by the multipole parameters. In contrast to the deformation density, it does not

involve the subtraction of an arbitrary spherical model.

Figure 3.13 shows a trajectory plot of the first derivative of the electron density. This graph shows how the structure can be naturally divided into individual *atomic basins*. *Bond paths*, which are shown as black lines, are drawn along the trajectories of maximum electron density inbetween two nuclei. *Bond critical points*, which are defined by a saddle point in the electron density along the bond path, are shown as blue dots and mark the border between two atoms. This graph confirms that atoms in molecules are not spherical, but can have different shapes based on electronegativity and properties of surrounding atoms.

An analysis was performed on the individual bond critical points. The results are displayed in table 3.3. The properties of the $C-O$ bonds and $H \cdots O$ bonds agree with values obtained by Overgaard et al. and Espinosa et al. [29, 30]

The distance between a bond critical point and both of its corresponding atoms (d_i, d_j) is an indication of the polarity of the bond. These data show that for all bonds, the location of the bond critical point is shifted towards the more electropositive element. This effect is for example much stronger for $O-H$ bonds than for $C-O$ bonds, which indicates that the former are more polar.

The Laplacian of the electron density at the bond critical point ($\nabla^2\rho$ BCP) is an indication of the type of bond and its strength, where a greater absolute value indicates a stronger interaction. A negative value represents a covalent bond, whereas a positive value represents a closed shell interaction. These data confirm that a shorter bond corresponds to a stronger interaction. A Laplacian plot in the plane of the formate ion is shown in figure 3.14. This plot shows the shared interactions between carbon and its surrounding atoms and suggests valence shell charge concentration on the oxygen atoms.
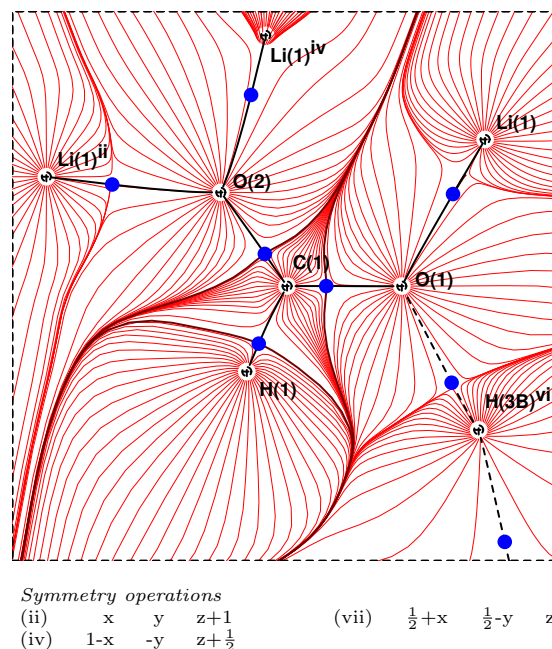

Symmetry operations
(ii)   x   y   z+1   (vii) $\frac{1}{2}$+x $\frac{1}{2}$-y   z
(iv)   1-x   -y   z+$\frac{1}{2}$

Figure 3.13: Gradient vector plot dividing the compound into atomic basins

Table 3.3: Results of bond critical point analysis

i		j	d_i (Å)	d_j (Å)	d_{ij} (Å)	$\nabla^2\rho$ BCP
C(1)	—	O(1)	0.4308	0.8231	1.2539	-29.76(8)
C(1)	—	O(2)	0.4264	0.8277	1.2540	-27.47(7)
C(1)	—	H(1)	0.6828	0.3507	1.0335	-20.81(6)
O(3)	—	H(3A)	0.7142	0.1971	0.9113	-39.45(16)
O(3)	—	H(3B)	0.7190	0.1878	0.9068	-34.22(16)
Li(1)	—	O(1)	0.7395	1.2007	1.9402	4.864(1)
Li(1)	—	O(2)$^{\text{i}}$	0.7371	1.1828	1.9199	5.028(1)
Li(1)	—	O(2)$^{\text{iii}}$	0.7506	1.2062	1.9569	4.478(1)
Li(1)	—	O(3)	0.7565	1.2120	1.9684	4.363(1)
H(3A)	$\cdots$	O(3)$^{\text{v}}$	1.2619	0.7051	1.9670	2.839(2)
H(3B)	$\cdots$	O(1)$^{\text{vi}}$	1.1788	0.6275	1.8063	3.664(8)

Symmetry operations

(i)	x	y	z-1		(iii)	1-x	-y	z-$\frac{1}{2}$		(vi)	x-$\frac{1}{2}$	$\frac{1}{2}$-y	z
(ii)	x	y	z+1		(v)	1-x	1-y	z-$\frac{1}{2}$					

- - Positive $\nabla^2\rho$
— Negative $\nabla^2\rho$
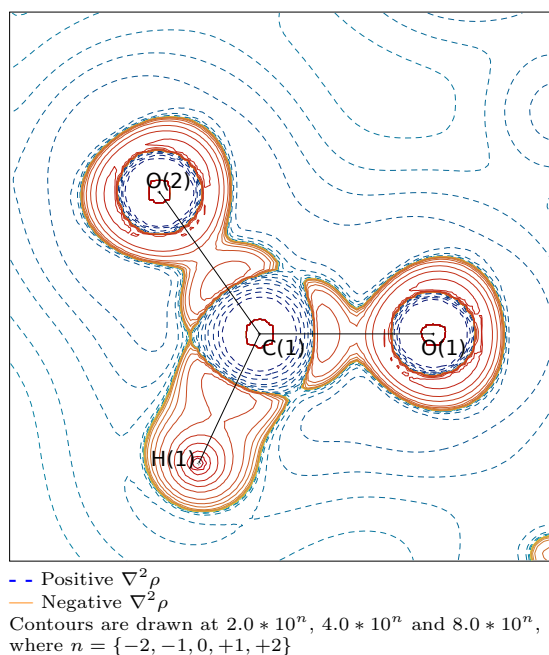Contours are drawn at $2.0 * 10^n$, $4.0 * 10^n$ and $8.0 * 10^n$, where $n = \{-2, -1, 0, +1, +2\}$

Figure 3.14: Laplacian of the electron density ($\nabla^2\rho$) in the plane of the formate moiety

3.3.5 Atom charges

Charges of individual atoms were calculated in three different ways, as seen in table 3.4. The *monopole* charges are a result of the refinement process and do not bear significant physical relevance. The *stockholder* method makes use of a Hirshfeld population analysis. [31] With the final method, *Atoms in Molecules*, the charges are determined by integrating the electron density in the atomic basins, as described in section 3.3.4. The AIM charges in particular closely resemble intuitive charge distributions, where oxygen atoms carry a strong negative charge and carbon and lithium atoms carry a positive charge.

Table 3.4: Individual atom charges (a.u.) by method

Atom	Monopole	Stockholder	AIM
O(1)	-0.253(15)	-0.238	-1.256
O(2)	-0.250(14)	-0.233	-1.287
O(3)	-0.436(17)	-0.166	-1.178
C(1)	-0.36(4)	+0.227	+1.746
Li(1)	+0.655(17)	+0.125	+0.795
H(1)	+0.186(18)	+0.052	+0.020
H(3A)	+0.198(11)	+0.119	+0.584
H(3B)	+0.264(11)	+0.113	+0.549

4

Conclusions and outlook

State-of-the-art technology allows crystallographers to aquire much higher quality data than what was possible in the early days of research on this compound. Since then, developers have released a great variety of software packages for different crystallographic applications, such as peak processing, structure refinement and extensive structural analyses. This ultimately provides the possibility to practically gain quantum mechanical insight in the electron distribution in a crystal, using only X-ray diffraction data. It also enables one to distinguish subtle structural details, such as the orientation of a polar axis.

Due to the polar nature of the $C - O$ bonds in this compound, the magnitude of the Laplacian of the electron density at the bond critical points is very sensitive to changes in the refinement process. This is an indication that the used multipole model may be approaching its limits. Furthermore, the polymeric character of the structure makes it difficult to accurately determine the hydrogen positions and displacement parameters using a rigid body model. It turns out that the atomic charges are very sensitive to the hydrogen positions and displacement parameters.

The current results can be relevant for understanding the nonlinear optical properties that this crystal shows, such as second harmonic generation, in which atom charges and the polarity of the crystal play an important role. Also, the acquired data can potentially be used for comparison with quantum mechanical calculations in future studies, to get a better understanding of the physical relevance of the current results.

Bibliography

[1] S. Singh, W. A. Bonner, J. R. Potopowicz, and L. G. Van Uitert. Nonlinear optical susceptibility of lithium formate monohydrate. *Applied Physics Letters*, 17(7):292–294, 1970.

[2] S. Lelie, E.O. Hole, M. Duchateau, W. Schroeyers, S. Schreurs, and D. Verellen. The investigation of lithium formate hydrate, sodium dithionate and n-methyl taurine as clinical {EPR} dosimeters. In *Radiation Measurements* [2], pages 218 – 224.

[3] André Krivokapić, Siv G. Aalbergsjø, Hendrik De Cooman, Eli Olaug Hole, William H. Nelson, and Einar Sagstuen. Lithium formate for epr dosimetry: Radiation-induced radical trapping at low temperatures. *Radiation Research*, 181(5):503–511, 2014. PMID: 24720752.

[4] André Krivokapić, Audun Sanderud, Siv G. Aalbergsjø, Eli Olaug Hole, and Einar Sagstuen. Lithium formate for epr dosimetry (2): Secondary radicals in x-irradiated crystals. *Radiation Research*, 183(6):675–683, 2015. PMID: 26010706.

[5] JK Mohana Rao and MA Viswamitra. Crystal structure of piezoelectric lithium formate monohydrate. *Ferroelectrics*, 2(1):209–216, 1971.

[6] A. Enders-Beumer and S. Harkema. The crystal structure of lithium formate monohydrate. *Acta Crystallographica Section B*, 29(4):682–685, Apr 1973.

[7] J. O. Thomas, R. Tellgren, and J. Almlöf. Hydrogen bond studies. xcvi. x–n maps and *ab initio* mo–lcao–scf calculations of the difference electron density in noncentrosymmetric lithium formate monohydrate, lihcoo.h$_2$o. *Acta Crystallographica Section B*, 31(7):1946–1955, Jul 1975.

[8] S. Harkema, G. de With, and J. C. Keute. Lithium formate monohydrate: a comparison of the x–n difference density and structural parameters derived from different experiments. *Acta Crystallographica Section B*, 33(12):3971–3973, Dec 1977.

[9] J. O. Thomas. X–n and multipole deformation electron density maps for the non-centrosymmetric structure lithium formate monohydrate, lihcoo.h$_2$o. *Acta Crystallographica Section A*, 34(5):819–823, Sep 1978.

[10] P. Coppens. Some implications of combined x-ray and neutron diffraction studies. *Acta Crystallographica Section B*, 30(2):255–261, Feb 1974.

[11] M. A. Spackman and P. G. Byrom. Retrieval of structure-factor phases in non-centrosymmetric space groups. model studies using multipole refinements. *Acta Crystallographica Section B*, 53(3):553–564, Jun 1997.

[12] T. Kottke and D. Stalke. Crystal handling at low temperatures. *Journal of Applied Crystallography*, 26(4):615–619, Aug 1993.

[13] Antoine M. M. Schreurs. Peakref. *Utrecht University, The Netherlands*, 2005.

[14] Antoine M. M. Schreurs, Xinyi Xian, and Loes M. J. Kroon-Batenburg. *EVAL15*: a diffraction data integration method based on *ab initio* predicted profiles. *Journal of Applied Crystallography*, 43(1):70–82, Feb 2010.

[15] George M. Sheldrick. Sadabs. *Universität Göttingen, Germany*, 2008.

[16] George M. Sheldrick. Crystal structure refinement with *shelxl*. *Acta Crystallographica Section C*, 71(1):3–8, Jan 2015.

[17] Bruker. Saint. *Bruker AXS Inc., Madison, Wisconsin, USA*, 2007.

[18] A Volkov, P Macchi, LJ Farrugia, C Gatti, P Mallinson, T Richter, and T Koritsanszky. Xd2006–a computer program package for multipole refinement, topological analysis of charge densities and evaluation of intermolecular energies from experimental and theoretical structure factors. *Program Version*, 5, 2006.

[19] Robert F. Stewart, Ernest R. Davidson, and William T. Simpson. Coherent xray scattering for the hydrogen atom in the hydrogen molecule. *The Journal of Chemical Physics*, 42(9):3175–3187, 1965.

[20] Robert F. Stewart, John Bentley, and Bernard Goodman. Generalized xray scattering factors in diatomic molecules. *The Journal of Chemical Physics*, 63(9):3786–3793, 1975.

[21] N. K. Hansen and P. Coppens. Testing aspherical atom refinements on small-molecule data sets. *Acta Crystallographica Section A*, 34(6):909–921, Nov 1978.

[22] Enrico Clementi and Carla Roetti. Roothaan-hartree-fock atomic wavefunctions: Basis functions and their coefficients for ground and certain excited states of neutral and ionized atoms, z54. *Atomic Data and Nuclear Data Tables*, 14(34):177 – 478, 1974.

[23] J. Salud, M. Barrio, D. O. López, J. Ll. Tamarit, and X. Alcobé. Anisotropy of intermolecular interactions from the study of the thermal-expansion tensor. *Journal of Applied Crystallography*, 31(5):748–757, Oct 1998.

[24] H. D. Flack and U. Shmueli. The mean-square friedel intensity difference in *p*1 with a centrosymmetric substructure. *Acta Crystallographica Section A*, 63(3):257–265, May 2007.

[25] Martin Lutz and Antoine M. M. Schreurs. Was bijvoet right? sodium rubidium (+)-tartrate tetrahydrate revisited. *Acta Crystallographica Section C*, 64(8):m296–m299, Aug 2008.

[26] Rob W. W. Hooft, Leo H. Straver, and Anthony L. Spek. Determination of absolute structure using bayesian statistics on bijvoet differences. *Journal of Applied Crystallography*, 41(1):96–103, Feb 2008.

[27] Anthony L. Spek. Structure validation in chemical crystallography. *Acta Crystallographica Section D*, 65(2):148–155, Feb 2009.

[28] R. H. Blessing. An empirical correction for absorption anisotropy. *Acta Crystallographica Section A*, 51(1):33–38, Jan 1995.

[29] Jacob Overgaard, Finn K. Larsen, Grigore A. Timco, and Bo B. Iversen. Experimental charge density in an oxidized trinuclear iron complex using 15 k synchrotron and 100 k conventional single-crystal x-ray diffraction. *Dalton Trans.*, pages 664–671, 2009.

[30] E. Espinosa, M. Souhassou, H. Lachekar, and C. Lecomte. Topological analysis of the electron density in hydrogen bonds. *Acta Crystallographica Section B*, 55(4):563–572, Aug 1999.

[31] F.L. Hirshfeld. Bonded-atom fragments for describing molecular charge densities. *Theoretica chimica acta*, 44(2):129–138, 1977.